CMS HCAL Hybrid Photodiode Design and Quality Assurance Stations

Priscilla B. Cushman and Adriaan H. Heering

University of Minnesota, Minneapolis, MN 55455

***Abstract*- The hadronic calorimeter for the CMS experiment requires photodetection in a 4 Tesla magnetic field. This, plus high neutron radiation and a 25 ns bunch-crossing, necessitated the development of a new type of high-rate multi-channel hybrid photodiode. As our specifications became tighter, design changes in the diode structure and surface treatment became necessary, resulting in a better product with very low crosstalk in both AC and DC modes. The specifications are rigorous and are maintained by a set of automated Quality Assurance stations which will process 570 tubes over 2 years.**

I. Introduction

The CMS Hadronic Calorimeter [1] is a sampling calorimeter composed of scintillating tiles alternating with brass absorber arranged in a projective tower geometry pointing back to the interaction region. Energy deposited in each active scintillator element produces blue light, a few percent of which is captured and re-emitted at ~520 nm in wavelength-shifting (WLS) fibers coiled inside the tiles. Clear fibers mated to the WLS fiber route the light to readout boxes located outside the calorimeter, but still within the 4 T solenoid field. The fibers are originally arranged by horizontal layer, arriving at the reaout box via fiber ribbon cables. They are sorted into bundles corresponding to towers within the readout box itself. The resulting fiber bundles are glued into holes in a black plastic PET (polyethylene terephthalate) disk with 19 or 73 of such bundle holes, each matching the position of an individual pixel on the face of a multi-channel Hybrid PhotoDiode (HPD). The entire assembly is fly-cut and polished, and pressed against the HPD optical faceplate with a spring-loaded, pin-aligned mounting jig as shown in Fig. 1. The bundles can have as few as 2 fibers and as many as 18, depending on the number of tiles stacked into a tower. The readout solution optimized cost per channel by providing 19 and 73-channel HPD's in identical housings and pin-out patterns, though a recent economic measure eliminated the thin compensation layer, and thus the 73-channel (2-3 fibers/bundle) version entirely.

II. Choice of Hybrid Photodiode Technology

The magnetic field constraint forced us to a silicon-based solution. This was quickly narrowed down to 2 possibilities: either a development project using multi-channel HPD's or individual avalanche photodiodes (APD's) of the same type proposed for our electromagnetic calorimeter, producing an integrated readout solution for the combined calorimeter. The decision was made by observing pions, electrons and muons from a tile/fiber calorimeter with both readout systems in a 1995 CERN test beam run [2,3]. The HPD response to MIP's as well as to the DC signal from the radioactive source calibration demonstrated a better signal-to-noise than the APD, despite the better quantum efficiency of the APD. The nuclear counter effect (background caused by muons depositing energy directly in the silicon) is reduced in a hybrid device by the additional factor of gain enjoyed by the photoelectrons of the true signal. Unlike the CMS ECAL which requires compact, individual transducers on each crystal, the HCAL fibers could be arranged in multi-pixel format, leading to a less expensive solution. Since the HPD signal response was uniform over the tube and the current is very low, many channels could be driven by one HV supply and bias. Overall, the HPD system was easier to use, less expensive, and more stable with respect to temperature and bias voltage.

III. Custom Tube Design

A development project was therefore initiated with DEP[1] to produce a tube which fully met the CMS criteria. A photograph of the final tube and internal diode array are found in Fig. 2. The diagram in Fig. 3 shows all the salient

[1] B.V. Delft Electronische Producten, Roden, Netherlands

features of the tube and internal diode in its final form. The following changes to the commercially available 7-channel tube design existing in 1995 were necessary in order to produce this product:

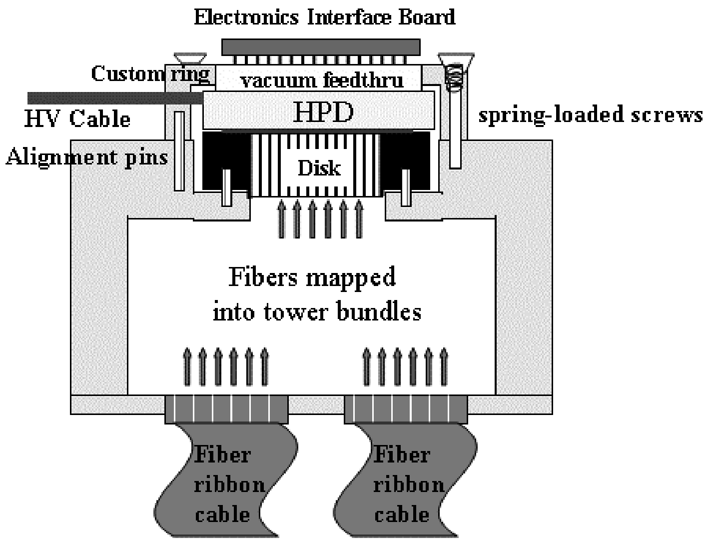

Fig. 1. The HPD is mounted in a readout box which decodes the fibers into tower bundles. The plastic disk which presents the fiber bundles to the HPD faceplate is spring-loaded. Alignment is done during quality assurance, producing custom rings for each HPD, such that the readout box and disk can be universal.

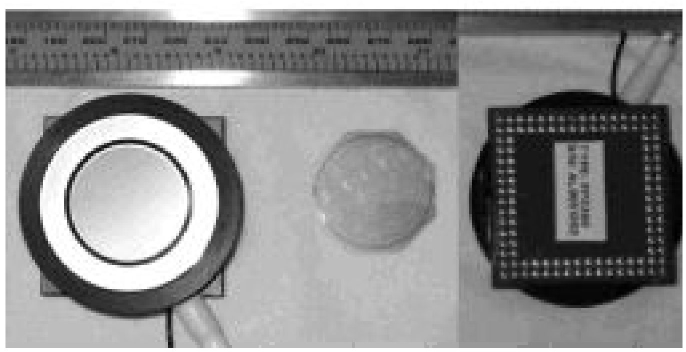

Fig. 2. The front and back of the CMS HPD are shown to the left and right of the 19-channel hexagonal close-packed diode array which is mounted inside.

1) *Reduction in the accelerating gap*

Extensive studies performed in a 5 Tesla, 30 cm bore MRI solenoid confirmed that the tube could handle repeated cycling in the field without damage, despite the presence of the Kovar ring used in brazing the tube [4]. The major effect of an off-axis tilt is a simple image shift due to E x B. Second-order off-axis effects include a cosine reduction in response due to a longer path length through the dead surface layer of the diode (thus raising the effective threshold) [5]. The gap was reduced from 5.3 mm to 3.3 mm to minimize image shift and its size was verified by angular studies in the magnet. A narrower gap relaxed tolerances on alignment of the tubes parallel to the B-field to 2^o, such that optical crosstalk due to image shift was eliminated, as long as 400 μm was maintained between the edges of fiber bundles. Even smaller accelerating gaps were rejected as posing too high a risk of high voltage breakdown, since a gain of 2500 requires a 12 kV operating voltage over 10 years of CMS running.

2) *Larger surface area*

The area was enlarged in order to accommodate the larger fiber bundles along with an additional 400 μm of space between bundles. This additional space is needed not only to prevent optical crosstalk between pixels in the event of a non-parallel alignment of tube axis with magnetic field, but also in order to maintain the mechanical integrity of the plastic disk which presents the fiber bundles to the face of the tube. The 487 mm^2 active area is realized by increasing the window diameter of a nominal 25 mm format tube to 27 mm, putting the perimeter of the active area closer to the walls of the tube than had ever been attempted before, raising concerns about charging of the body walls. Space charge effects were not a problem; instead, the tight space made potting difficult and was responsible for high voltage breakdown in a subset of tubes.

3) *New HV feedthru designs to improve reliability.*

Interior sparking to photocathode can cause sudden death, as well as slow deterioration in photocathode response as pinholes are temporarily created in the fiber optic faceplate, slightly spoiling the vacuum before annealing again. Current spike monitoring stations were developed to detect the onset of sparking before deterioration. They also helped identify the problem, which was then eliminated by potting techniques to reduce voids, and by increasing the insulation between the interior ground and photocathode. The cable sheath is embedded in the tube potting and extends out over the exterior cable in order to provide mechanical support.

4) *Smaller, denser packing of the pixels.*

Optimization of channel cost for the HCAL tower geometry, moderated by the magnetic field tolerances discussed above, led to a close-packed hexagonal array of 5.4 mm flat-to-flat pixels for towers with large bundles (19-channel version) and 2.68 mm flat-to-flat pixels for small bundles (73-channel version). These arrays map to each other in such a way that the same vacuum feedthru design can be used for both, thus reducing the design cost of this component.

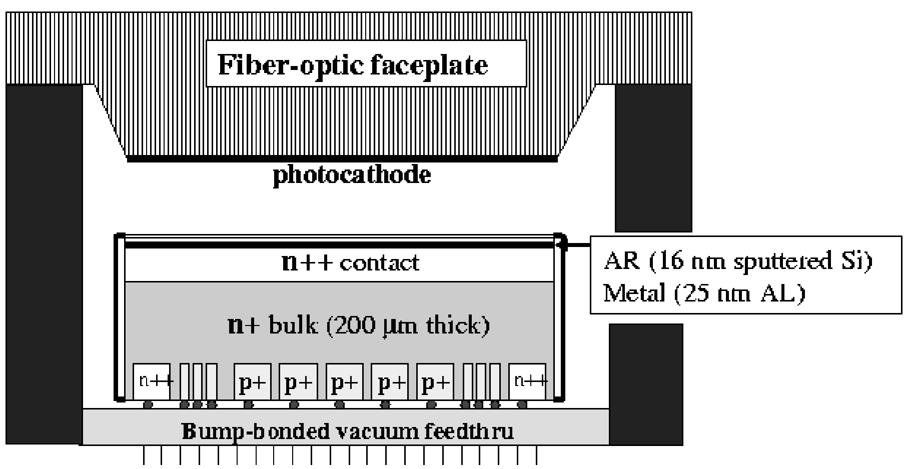

Fig. 3. Representation of the custom CMS diode array internal structure and its installation in a proximity-focussed vacuum tube. Not to scale.

5) *New ceramic vacuum feedthru design*

The 73-channel device required denser pixel arrangements than ever before achieved by DEP. Work sponsored by the SSC project showed that Litton[2] could produce multi-channel hybrid avalanche photodiodes [6] with dense pixel structure by indium bump-bonding to gold pads on a ceramic feedthru. DEP's first tubes were wire-bonded. During the high heat of photocathode processing, several pixels would frequently lose their contact or diffusion of the thin aluminum contact layer into the silicon would cause locally high leakage currents. A failed attempt by DEP to produce their own glass feedthru convinced them to follow Litton's lead. They sub-contracted with Kyocera[3] to design the multi-layer ceramic feedthru, which transfers signals from a hexagonal array of bump-bonds to a standard 0.1" pitch pin grid array (see right-hand photo in Fig. 2). In the assembly of the readout box, these pins fit to a standard zero insertion force (ZIF) socket with a locking lever. In order to assure the reliability of these contacts, the

[2] Litton Electro-Optical Systems, 1215 52nd St., Tempe, AZ 85281, USA
[3] Kyocera Corporation (Fine Ceramics Division), Kyoto, Japan

pins were gold-plated. A study conducted at DEP proved that the diffusion of gold into the Kovar pins during module brazing was not a problem.

6) *Optimization of the photocathode*

An S20 photocathode is applied to a Schott[4] glass fiber optic window (6 µm fibers). The quantum efficiency is 11%-18% at 520 nm with a broad wavelength maximum. Care is taken to keep the red sensitivity low since this translates into increased dark counts. Tubes have dark counts at rates from 0.5 kHz/cm^2 for quantum efficiencies of 0.2% (800 nm) up to a MHz/cm^2 for one tube with 2.8% (800 nm) quantum efficiency.

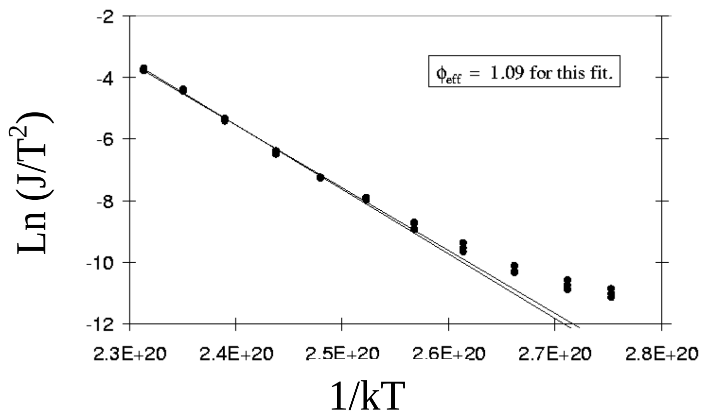

Fig. 4. The number of individually counted dark counts per pixel from the photocathode of a sample 73-channel HPD as a function of temperature, plotted such that the slope gives the work function according to the Richardson-Dushman equation. Several runs were taken and the fits are also shown.

Work functions, Φ, of the photocathodes were obtained by fitting the Richardson-Dushman equation [7]:

$$J(T) = A\,T^2 \exp\left(-\frac{\Phi_{eff}}{kT}\right)$$

where T is the temperature, k is the Boltzmann constant, A=1.2x10^6 A/m^{2}K^2 is the Richardson constant and J(T) is the dark current density. The work function is extracted from Φ_{eff}

$$\Phi_{eff} = \Phi - \sqrt{Ee^3 / 4\pi\varepsilon_o}$$

where the applied field E = 2750 kV/m and e is the electron charge. Fits were performed for photocathodes at temperatures down to –10^o C using an aluminum box coupled to a Peltier cooler, finding Φ of 1 to 1.33 eV. Micro-sparking in earlier tubes produced a departure from the Richardson-Dushman equation at low temperatures, representing a constant, low background. The sparks produced light (as measured by a PMT pressed against the HPD faceplate), the rate of which depended on the applied high voltage.

IV. DIODE DESIGN

The silicon diode is fabricated using epitaxial growth by Canberra[5] with the basic structure outlined in Fig. 3. The photoelectrons are converted to electron-hole pairs within the first few micrometers of the surface of the lightly-doped (n+) bulk n-type layer. The holes drift through the silicon and are collected from the backside p+ implants, which define a hexagonal close-packed array of pixels. Additional p+ structures on the back define a grounded ring plus six floating guard rings that maintain uniformity for the edge pixels and aid in maintaining a high breakdown voltage. At the edge of the diode, there is an n++ ring, which supplies the bias voltage from the back of the diode to the front n++ surface through the bulk material. There are 40 microns between each pixel implant, but no dead space in the response uniformity.

[4] Schott Fiber Optics Inc, 122 Charlton St, Southbridge, MA 01550, USA
[5] Canberra Semiconductor N.V., Lammerdries 25, B2250, Olen, Belgium

The shape of the output pulse in response to a delta function input pulse, reveals much about the internal structure of the diode. The rising and falling edges are defined by the RC constant of the combined diode plus preamplifier and connections, whereas the central region is determined by the drift speed of the holes [8]. Thus, the slope of the mid-region of the pulse shape mirrors the internal E-field generated within the diode as a function of x through the bulk in our simple model, similar to treatments for silicon trackers [9]:

$$E(x) = \frac{2V_d x}{d^2} + \frac{(V_b - V_d)}{d}$$

where d is the diode thickness, V_d is the depletion voltage, and V_b is the applied bias. Integrating to get the current:

$$I(t) = e^{\frac{2\mu V_d}{d^2}t} Nq\mu(V_b - V_d)/d^2$$

where Nq is the total charge generated within the depleted region and μ is the hole mobility, μ.= (1/E) dx/dt = 450 cm^2/Vs. The plateau of the pulse is flat for low depletion voltages or thick diodes, where the exponent in the current is small. The output current pulse has a width given by the time Δ(ns) for a hole to travel distance d:

$$\Delta(ns) = d^2 \ \ln\left(\frac{\sqrt{V_b + V_d}}{\sqrt{V_b - V_d}}\right)/\mu V_d$$

In Fig. 5, scope traces of the response to a 1.5 ns pulse from a light-emitting diode (LED) show how the structure of the diode has changed over our development period. The conventional 300 μm thick silicon gave wider than optimum pulses for the CMS application. Reversing the diode doping scheme in order to drift the faster mobility electrons would have necessitated a new (and expensive) development project with Canberra, so instead, we decided to reduce the wafer thickness to 200 μm in order to reduce d in the above equations. Despite the increased fragility of the wafers, the loss in yield has been negligible.

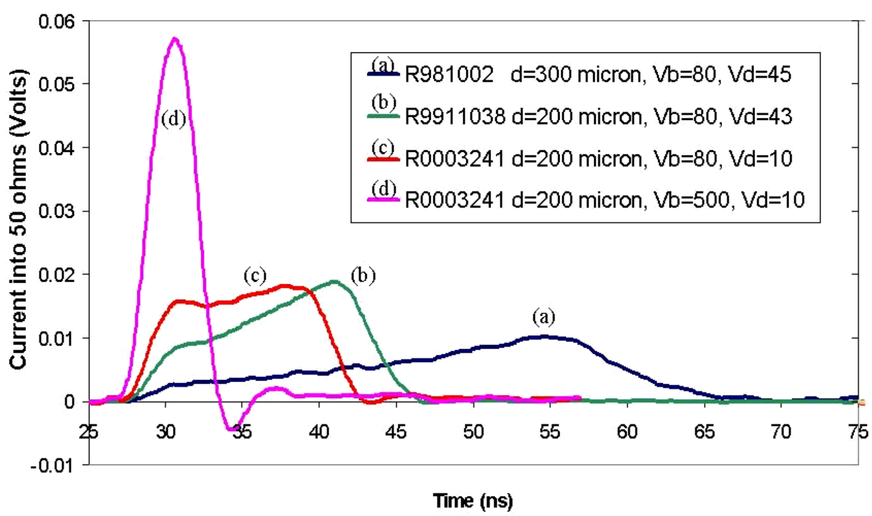

Fig. 5. Pulse shapes for (a) the 300 micron and (b) the 200 micron diodes at 80 V bias, (c) the low-depletion, 200 micron diodes at 80 V bias and (d) the low-depletion, 200 micron diodes at 500 V bias.

A further improvement in pulse width can be obtained by insisting on higher resistivity silicon, which pushes down the depletion voltage. In Fig. 5, the pulse shapes from later diodes (c) clearly show a flatter plateau and narrower width at the operating voltage of 80 V. Once the depletion voltage is small compared to the bias, the output pulse becomes square with its width Δ(ns) ~ $d^2/\mu V_b$ and its height maintaining the total area via h(nA) ~ Nq/Δ. The later diodes were also able to tolerate much higher reverse bias without breaking down, and so could be operated in a highly depleted mode: see the very narrow pulse (d) in Fig. 5 at a bias of 500 V.

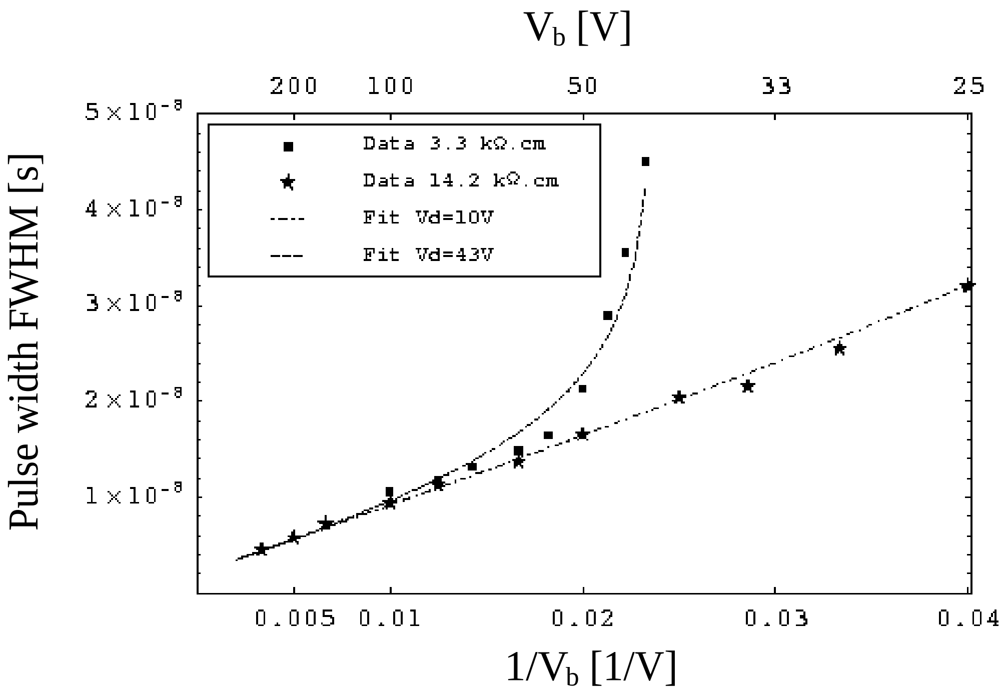

Fig. 6. Pulse width versus inverse bias voltage. Data (squares) from the earlier diodes fitted to the above model for pulse width, shows that the width diverges quickly below the operating bias of 80 V, whereas the new diodes (stars) with lower depletion voltage have a 'linear' behavior as the voltage is decreased.

Using the above model, fits to the pulse width as a function of inverse applied bias in Fig. 6 show that the low depletion diodes produce stable pulse shapes at the operating bias voltage of 80 V, whereas higher depletion voltages can be affected by variations in the delivered bias. We therefore specified a minimum resistivity of 5 kΩ-cm, corresponding to $V_d < 30$ V for d = 200 μm and an electron mobility (according to Canberra) of 1350 cm^2/Vs. We specify a maximum depletion voltage of 35 V to accommodate the tolerance in the diode thickness. The capacitance per pixel when depleted is measured to be <5 pF/pixel for the 73-channel device and 16 pF/pixel for the 19-channel diode.

V. CROSSTALK

1) AC Capacitive Crosstalk

As work progressed on implementing the fast electronics required for the CMS readout, we discovered differential crosstalk between pixels that depended on the speed of the charge integration. This was not noticed when using the slower preamplifiers and gated ADC's of the test beam. The 300 ohms/sq resistivity across the 100 nm thick upper n++ layer and the 300 ohms resistance from back n++ bias contact to the front, provided insufficient current to respond to the faster pulses and shorter integration time, thus draining the neighboring pixels. A large negative-going pulse in Fig. 7(b) is induced in a side pixel of the bare silicon 19-channel HPD when the central pixel (the positive trace (a) shown at 1% of its actual size) is illuminated. There is not much radial dependence in this differential crosstalk, so that even though it is only 2.5% per pixel (1% per pixel for the 73-channel tube), it adds up to 50 % over the whole tube. This is AC crosstalk, in that it only shows up for fast pulses and has its largest effect on tube performance in high rate experiments.

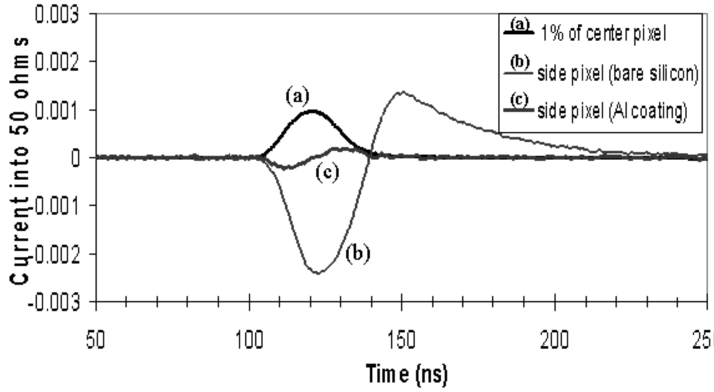

Fig. 7. AC cross-talk observed in (b) the side pixel of a bare silicon 19-channel HPD when (a) the input signal is in the center pixel. Reduction of this component for the aluminized HPD is also shown in curve (c).

The AC crosstalk was reduced to < 4% over the whole tube by applying a thin (25 nm) aluminum layer over the entire front surface. This reduced the resistivity to ~1 ohms/sq. Conduction was extended to the back bias contacts via 100 nm thick aluminum traces at two edges of the diode. After high leakage currents in some diodes indicated that diffusion of aluminum into the silicon was occurring during module brazing, a SiO_2 barrier layer was introduced between them. This barrier layer meant there was no longer a direct contact between the aluminum and n+ layer, but the capacitive coupling was sufficient to maintain charge delivery to the individual pixels at high rate operation and the leakage current drained through the bulk silicon. Canberra also demonstrated low leakage currents without a barrier layer by doping the aluminum itself with 1% silicon. The middle trace (c) in Fig. 7 demonstrates how the AC crosstalk has been made negligible by the aluminization.

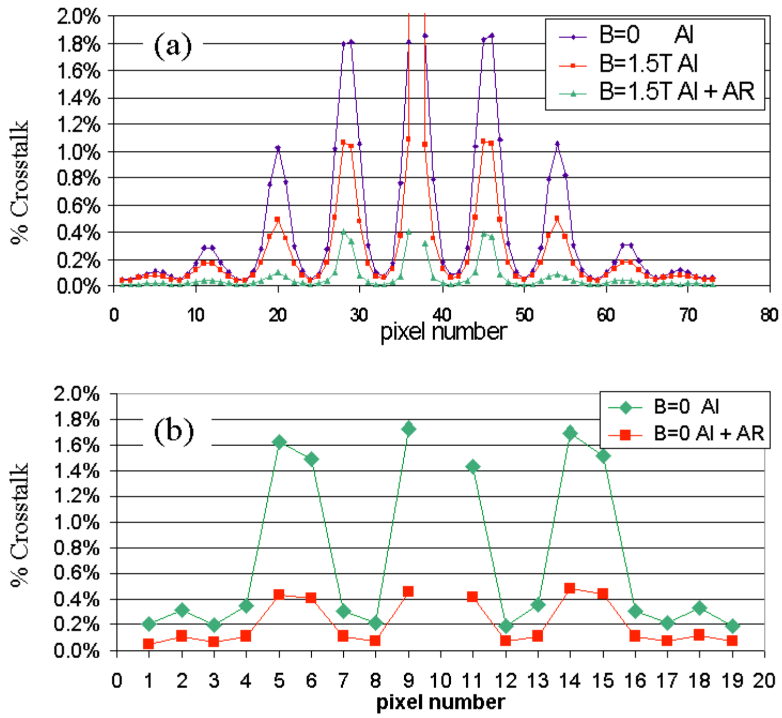

Fig. 8. (a) The combined backscatter and optical crosstalk (B=0) across an entire 73-channel HPD compared to the remaining optical reflection crosstalk once the field is turned on (B=1.5 T). The lowest crosstalk is for the tube with an anti-reflective coating over the aluminized layer. Light is injected into the central pixel, number 37. (b) The combined crosstalk (B=0) across a 19-channel HPD for the aluminized tube compared to the backscatter-only crosstalk once the anti-reflective (AR) coating has removed the optical component.

2) Optical Crosstalk

Removing the negative AC crosstalk revealed positive crosstalk which had previous been masked by the AC effect. Ironically, that positive crosstalk had been worsened by the addition of aluminum. If this crosstalk is caused only by backscattered electrons, then it can be eliminated by applying an axial magnetic field above 1 Tesla, since at that field strength, all electrons are focused back into the same pixel. As can be seen from the second curve in Fig. 8(a), a 1.5 T field has improved the situation, but there is still a low level of positive crosstalk remaining. This turns out to be light which is not converted by the photocathode. It reflects off the front surface of the diode, cannot be focused by the magnetic field, and has a second chance to produce photoelectrons when it again strikes the photocathode far from where it first entered. It is this optical crosstalk which is most adversely affected by the increased reflectivity of aluminum.

The radial dependence (Fig. 9) of the crosstalk in the first production 19-ch HPD was mapped by moving an illuminated 250 μm fiber across one pixel and reading out the adjacent pixel. In these plots, the origin corresponds to the pixel boundary and the value at 2.7 mm means that the fiber is in the center of the illuminated pixel. The B=1.5 T case represents almost purely optical crosstalk, shown in Fig. 10 as a fraction of the central current. No data at <0.5 mm is conclusive because a 1.5 T field with a back-scatter radius of 0.5 mm is used to subtract the optical component. In any case, no fiber will ever be closer than 0.8 mm to the boundary due to the construction of the cookies.

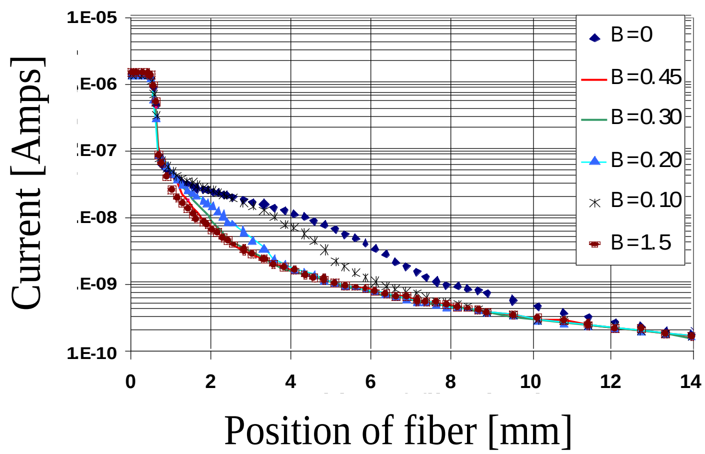

Fig.9 Raw crosstalk data for HPD AZ0139031

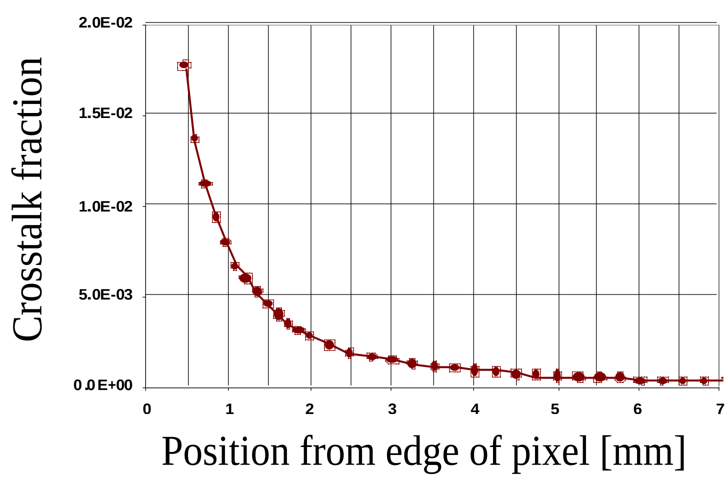

Fig. 10 Optical crosstalk component from 2nd bounce photoelectrons

The optical crosstalk curve was found to be completely consistent with a direct measurement of the reflected light off the internal diode using an avalanche photodiode on the surface of the HPD fiber optic faceplate, confirming that optical reflection is indeed responsible for crosstalk which survives in the presence of a high magnetic field. An interesting aside is that presumably all hybrid silicon devices have reflection crosstalk, since the reflectance of bare silicon at 40% is still significant, compared to 90% for our aluminum coating. This means that the true quantum efficiency of even a single channel HPD is less than the effective quantum efficiency, since the measured value always includes the reflection enhancement.

3) Back-scatter Crosstalk

By subtracting the B=1.5 T data (optical component) from all lower B-field data, we obtain the pure back-scatter distributions in Fig. 11. Since the radially symmetric back-scatter dependence is convoluted with an hexagonal pixel shape, the slope discontinuities represent true geometric effects.

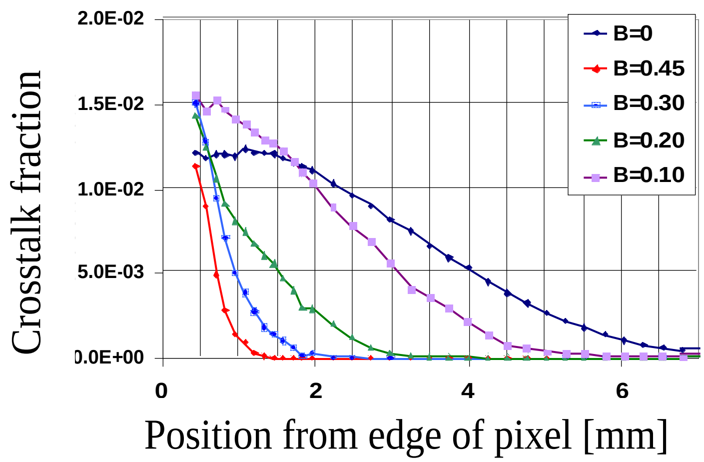

Fig. 11 Radial distribution of back-scatter crosstalk

From the Darlington paper [10], we expect 18% of the 10 keV electrons to be back-scattered with an average energy of 7 keV. The radial distance to impact point is dependent on the initial back-scattered angle: for B = 0, the maximum distance is when the initial angle is at 45 degrees and is given by 2d = 6.7 mm where d is the accelerating gap between photocathode and diode. For B=0.2 T and an initial angle of 0.65 radians, the electron comes back to the same place (radial distance = 0) after making one turn. For higher fields this becomes a spiral of multiple turns, thus causing multiple zeros, representing the particle returning to the origin. The radial intensity (Fig. 12 below) comes from this simple model

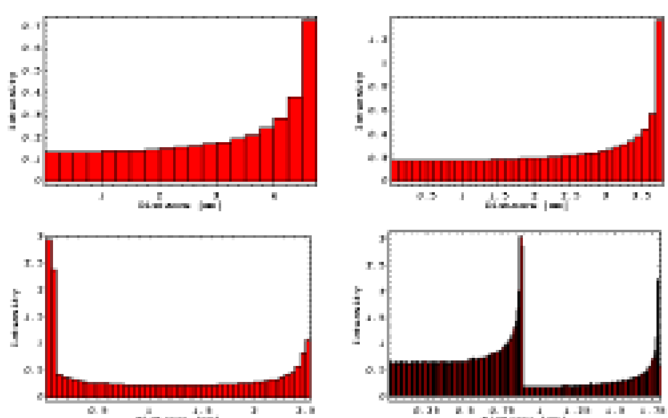

Fig.12.Balllistic Monte Carlo of radial back-scatter intensity for 7 keV electron at fields of B=0.0 T, B=0.1 T, B=0.2 T, B=0.3 T.

For B=0, this represents a fairly uniform disk of back-scatter (once the area of each increasing annulus is accounted for, as well as the blurring due to a range of energies) extending out to 5 mm on average (out to 6.7 mm for the max 10 keV). As the field is turned on, the disk shrinks and eventually at B = 0.2 T gets a second spike in the center from particles returning to the origin. Since the rim remains, however, moving a fiber slightly off-center results in a large increase in total crosstalk. When the field is off, the back-scatter disk is much larger than the pixel size and back-scatter crosstalk will be insensitive to where a fiber is located. Thus, fields of 0.1 T can actually be worse than no field at all, since crosstalk will now depend on which fiber in the bundle is lit up, whereas with zero field, the crosstalk is uniform and can be corrected by a simple factor.

VI. ANTI-REFLECTIVE COATING

In order to eliminate crosstalk due to reflection, we studied how to apply an anti-reflective coating to the front surface of the aluminum. We studied several options, including replacing the aluminum with silver, which would have provided both anti-reflection and AC crosstalk elimination in one thin layer, but oxidation made it far less stable. Other solutions with multiple metal layers produced unacceptably thick dead layers, thus increasing our threshold voltage and reducing our gain. Our choices were guided by an optical modeling package for multilayer structures called IMD[11]. In general, the thickness of the layers determines at which wavelength the minimum occurs, and the composition of the material determines the width and strength of the minimum. Our optimized formula called for 14 nm of hydrogenated amorphous silicon (a-Si:H) deposited over 25 nm of Al with a native layer of Al_2O_3 in between.

We made a series of test slides by plasma-enhanced chemical vapor deposition of a-Si:H (approximately 4% H by atomic weight) on glass slides with an initial 25 nm coating of aluminum. The thickness of the amorphous silicon layer was determined by varying the exposure time and comparing the resulting wavelength minimum with simulations using IMD. The slides were illuminated through a monochromator of 4 nm bandwidth. The reflected light was observed with a PIN diode in order to measure the reflectance as a function of wavelength and angle. The diode itself was also illuminated in the same position as the slide, and its wavelength response divided out. The system properly observed a flat response from a 99% reflectivity mirror and from the bare aluminized slide. The wavelength of the monochromator was checked with a calibrated filter. Our films matched the modeling program very well, as can be seen in Fig. 13.

DEP then tried to apply the same coatings, using a sputtering technique and non-hydrogenous amorphous silicon. Our calculations predicted that they should use 16 nm of a-Si to achieve the same wavelength minimum as 14 nm of a-Si:H. We measured their samples in the same setup used for our slides. Since their results depend on pressure, as well as other variables, it has been harder to come to a consistent picture. However, the DEP curve also shown in Fig. 13 can be reliably reproduced by DEP and provides adequate reduction in optical crosstalk at 520 nm. The thin layer of Al_2O_3 between aluminum and a-Si coating stabilizes the coating, which otherwise tends to disappear during tube processing via diffusion. In the end, it was unnecessary to apply this as a coating: merely exposing the aluminum surface to air for a short time was sufficient to create a native layer of Al_2O_3.

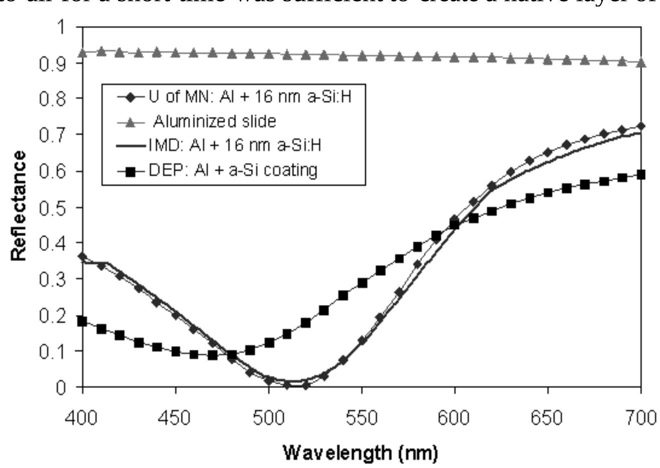

Fig. 13. 14 nm of a-Si:H deposited by PECVD on aluminized glass slides matches the IMD optical modeling program. The bare aluminized slide has an approximately flat response at 92%. The DEP sputtered a-Si, with a minimum of 475 nm gives adequate reflection crosstalk reduction, but could be better optimized.

Our success is measured in the crosstalk reduction finally obtained, for an acceptable increase in the thickness of the dead surface layer. After all surface treatments, the threshold voltage deduced by extrapolating the linear portion of the gain curve back to where it crosses the x-axis (see Fig. 20) went from a range of 500-1500V to 2000-2500V. The true threshold is overestimated by this procedure since a shallower slope in the gain is masked by an upturn in the quantum efficiency with voltage. The lowest curve in Fig. 8 (a) shows that the crosstalk in a 73-channel aluminized tube with anti-reflective coating is only 0.4 % into the nearest neighbors when the B-field removes the back-scatter component. It goes down to 0.1% at the next-nearest neighbors, which correspond to the nearest neighbors in the 19-channel tube. Fig. 8(b) shows the zero magnetic field case for the 19-channel tube, where back-scatter still contributes. The bottom curve shows the improvement due to the AR coating on that tube, effectively removing the optical component from the total crosstalk.

One can summarize the situation in Table I by quoting the total crosstalk in the whole tube. Recall that the crosstalk into any neighbor is below one percent, but the definition of “crosstalk” in Table I is the total amount of energy removed from the illuminated pixel into all other pixels. The components due to optical reflection and electron back-scatter can be isolated by making the same measurements in and out of a magnetic field. Since we operate at 4 T, the back-scatter component will be removed from consideration in the actual experiment, so the total crosstalk we will observe is within specifications and measured as 2-4%.

TABLE I: CROSSTALK
Percent removed from central pixel into all other pixels

Diode Type	Total % (B=0)	Optical % (B=1.5 T)	Backscatter % (B=0 – 1.5 T)
73-ch HPD			
Bare Silicon	18	7	11
Si + 25 nm Aluminum	29	16	13
Si + SiO_2 + Al + a-Si	10.4	2.4	8
19-ch HPD			
Bare Silicon	13.4	4.8	8.6
Si + SiO_2 + Al + a-Si	8.5	2.1	6.4

VII. QUALITY ASSURANCE

The final specifications are detailed in the contract with DEP (see Table II). The vendor is responsible for providing data on specifications 1, 4, 11, 12, 14, 15, 20, 21, 22. When the tubes arrive at the University of Minnesota, they are held for two weeks at 13 kV while current from the supply is monitored for sparking. Next the tubes go through an automated scanning station at a rate of one tube every 6 hours, transferring data to the CMS database on items 3, 5, 8, 10-17. Item 23 is checked with a Go/NoGo mechanical jig.

Besides uniformity scans, gain curves and leakage current maps, the scanning station also registers the position of the pixels within each HPD to 50 μm. An attached metal strip with 3 precisely-positioned 1 mm holes provides fiducial spots on the surface of the HPD when the focussed beam of light strikes the holes. The moveable platform translates the mounted HPD assembly in steps of 0.1 mm in x and y, to find the center of the light spots. These are then registered to the pixel intersection positions (above and below the metal strip in the same scan) via an automated iterative procedure using pixel response equalization. This provides a set of corrections in Δx, Δy, and θ to the standard mounting, which can then be used in machining the square hole in the mounting ring (see Fig. 1) which precisely registers the vacuum feedthru, and thus the tube as a whole. In this way, the disks, which hold the fiber bundles are simple inserts to the custom mounting ring and can be prepared ahead of time in batches and sent out to other institutions for fiber gluing, fly-cutting and assembly. A capacitance station measures capacitance and resistance as a function of bias voltage to determine the quality of the silicon and the depletion voltage, items 10-13.

TABLE II
SPECIFICATIONS FOR THE CMS HPD

PHOTOCATHODE (multi-alkali, glass FO)	*MIN*	*TYP*	*MAX*	*UNIT*
1. Quantum efficiency at 520nm	11	14		%
2. Dark counts			50	kHz/cm^2
3. Response non-uniformity			8	%
4. Operating voltage		12	13	-kV

PIN DIODE ARRAY	*MIN*	*TYP*	*MAX*	*UNIT*
5. Threshold for 10kev e^-	500	2500	3300	V
6. Thickness non-uniformity			±1	µm
7. Silicon resistivity	5			kΩ-cm
8. Response non-uniformity			10	%
9. Inter-pixel resistance	100			MΩ
10. Depletion depth	185	200	215	µm
11. Operating voltage	80	80		V
12. Breakdown voltage	100	150		V
13. Full depletion voltage		10	35	V
14. Guard ring reverse current			500	nA
15. Pixel reverse current		1	10	nA

TUBE PERFORMANCE	*MIN*	*TYP*	*MAX*	*UNIT*
16. Gain	2300	3300		e/pe
17. Gain non-linearity (1 - 70000 pe's)			5	%
18. Total optical crosstalk to sum of all pixels			4	%
19. Total capacitive crosstalk to all pixels			3	%
20. Full width half max at 80 V			20	ns
21. Baseline signal width maximum at 80 V			30	ns
22. Gap between photo-cathode and diode			3.55	mm
23. Carrier size tolerance within one batch			±40	µm

The tubes then undergo tests with pulsed light. Items 20-21 are addressed by observing sample pulse shapes and item 19 is addressed by an AC crosstalk test which compares the pulse in the illuminated pixel to 2 side pixels to determine if the aluminized coating and traces are thick enough (the resistance test also confirms this). Item 2 is addressed by taking pulse height spectra at low light levels using two 32-channel preamplifiers[6] serially read out through a voltage-sensing ADC. The microsecond shaping time gives individual photoelectron peaks, so that ion feedback or problems with the tube vacuum are easily flagged by observing the shape of the spectral tails. Optical crosstalk (item 18) is tested by measuring the current in all surrounding pixels when the central one is illuminated. The HPD is sandwiched between two disk magnets with a 0.3 T magnetic field, on order to remove the back-scattering component. A typical tube is characterized in Figures 14-21 in order to demonstrate the data which is available through the quality assurance system. These plots come directly from the maintained database and will eventually represent the largest statistical sample of HPD's ever characterized, helping to define yield and reliability for future experiments.

Selected tubes from each batch undergo lifetime testing after which the quality assurance procedure is repeated. The tubes must be able to operate for 10 years in a radiation field (mostly MeV neutrons), as well as handle integrated charge over that period as high as 3 C/pixel (off the anode) over a large bundle illuminating a 19-channel pixel at the most forward part of the barrel region [12]. Two 1 mm diameter WLS fibers are excited by blue LED's and read out on one end by calibrated reference PIN diodes. The other end is potted into a cookie and retracted slightly from the HPD window such that the entire pixel is illuminated. The LED's are set, one to deliver the maximum expected CMS charge in 10 months and the other to run at 1/10 the rate. The current from both reference diodes and the two HPD channels, as well as the temperature, are continuously monitored at time intervals of 30 minutes. In all 4 of the tubes observed so far, there is an increase in the effective quantum efficiency for the first 100 mC of charge, after which the response falls off at less than 1% per CMS year. Current spikes of greater than 100 nA will also trigger a reading in order to determine if internal sparking occurs. We also monitor the current off the high voltage supply.

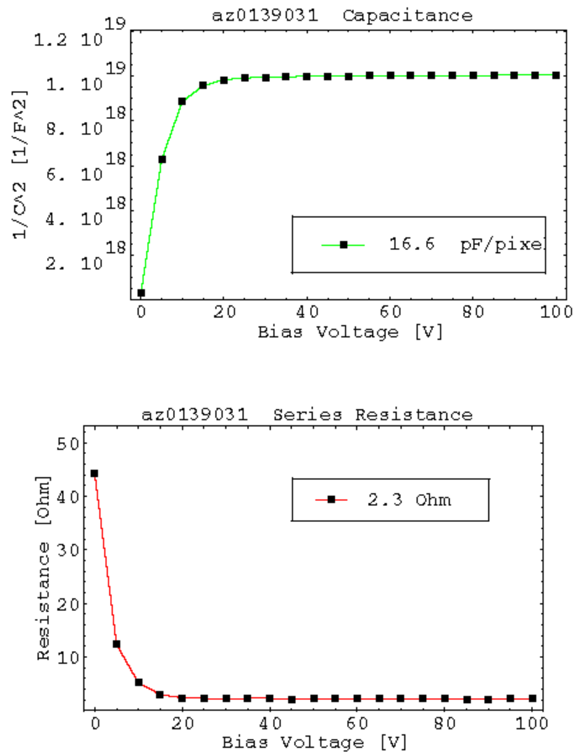

Fig. 14 Diode characterization in Capacitance Test Station

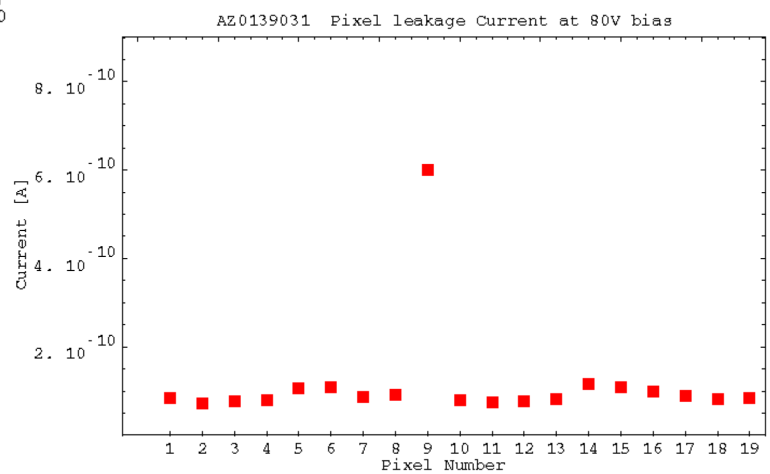

Fig. 15. Leakage Current per pixel at 80 volt reverse bias

A duplicate of this station resides outside a retractable drawer of the University of Minnesota Californium-252 irradiation facility. Quartz fibers link the LED-stimulated WLS fibers to the HPD inside the MeV neutron field and continue to monitor the tube response in situ as exposure proceeds. Radiation damage produces an increase in leakage current proportional to the dose. The aluminized 73-channel tube behaved in the same way as earlier tubes

[6] VA-Rich Viking chip. IDEAS, Hovik, Norway. http://www.ideas.no

[13]. Although the temperature was monitored, it was unnecessary to correct for it inside the thermally insulated concrete pile that houses the source. After a small increase in effective quantum efficiency, the main effect was an increase in leakage current corresponding to 50 nA over 4.5 x 10^{11} n/cm^2 effective integrated dose. The 19-channel pixels expect a factor of 4 more due to their larger area. The dose corresponds to approximately 100 CMS years in the worst section of the barrel.

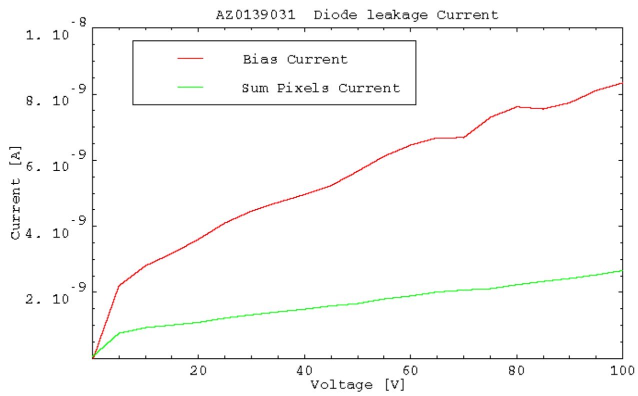

Fig. 16. Leakage current as a function of the bias voltage off supply (includes guard ring) and pixels tied together.

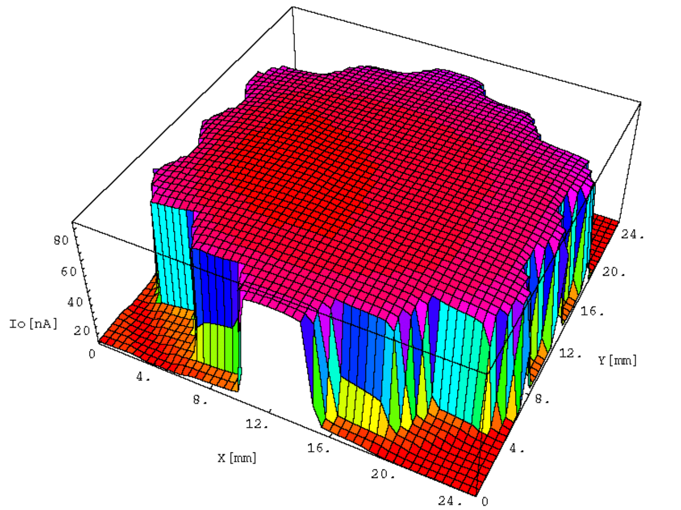

Fig. 17. DC scan of 19-ch HPD. No dead areas between pixels.

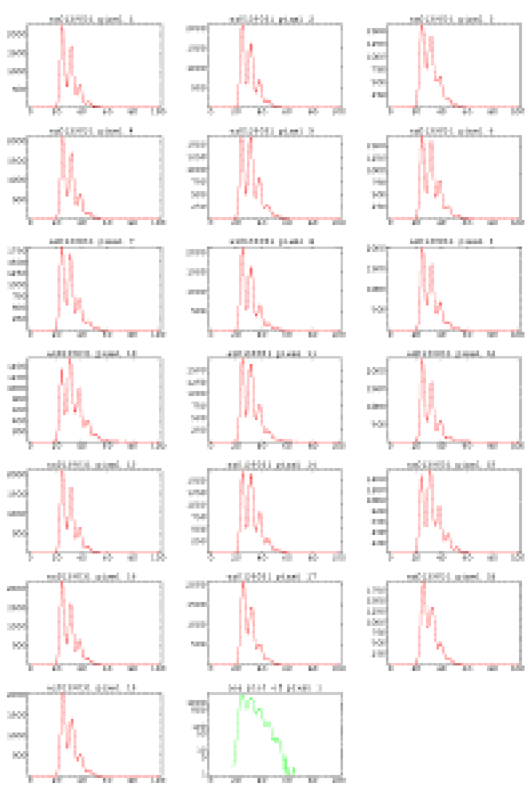

Fig. 18. Individual pulse height spectra for each channel and for the sum at low light levels. Viking AC setup.

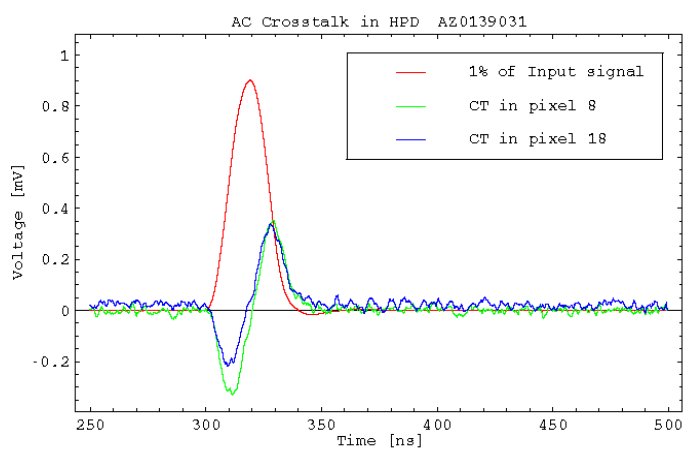

Fig 19. Capacitive AC crosstalk in selected pixels compared to 1% of actual signal in illuminated middle pixel.

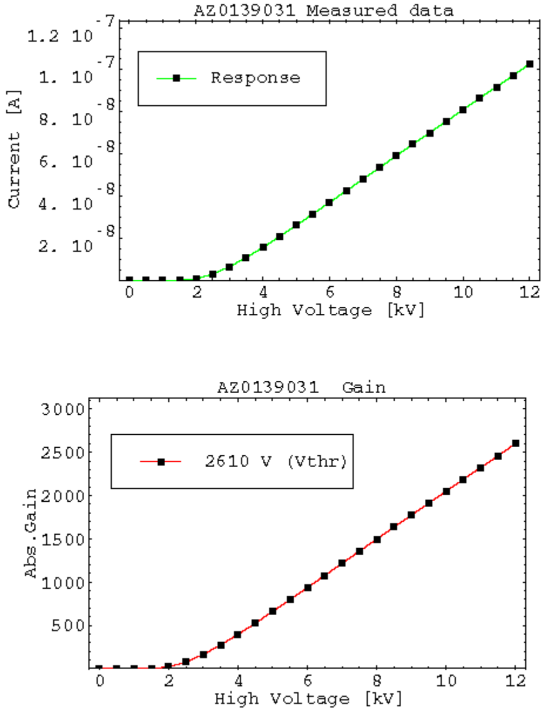

Fig. 20. Response curve and extracted absolute gain curve with, extrapolated threshold voltage. Since the quantum efficiency actually goes up with HV, the threshold is overestimated.

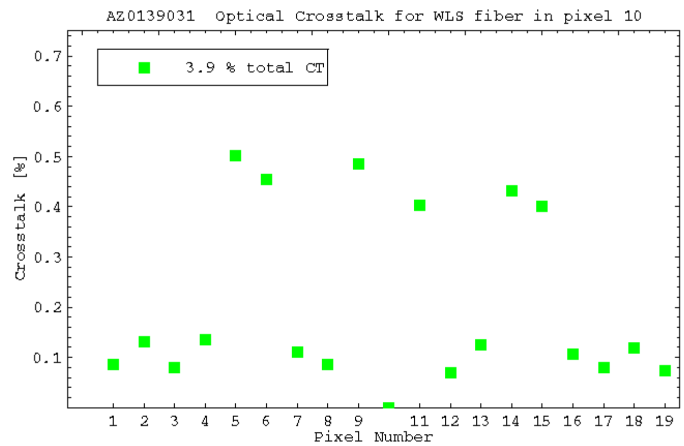

Fig. 21. Optical Crosstalk per pixel when central pixel is illuminated. DC test in a 0.3 T magnetic field.

VII. Acknowledgment

We thank Anatoly Ronzhin and Sergey Los for many interesting discussions, as well as the support of the entire US-CMS HCAL collaboration. We thank Bruce Hammer for the NMR magnet facility at the Center for Industrial Applications of Magnetic Resonance, Univ. of Minnesota. This work was supported in part by the U.S. Department of Energy under Grant DOE/DE-FG02-94ER40823

VIII. References

[1] CERN/LHCC 97-31, CMS TDR 2, 20 June 1997
[2] P. Cushman, A. Heering, J. Nelson, C. Timmermans, S.R. Dugad, S. Katta, S. Tonwar, “Multi-pixel hybrid photodiode tubes for the CMS hadron calorimeter,” Nucl. Instr. Meth. vol. A387, pp. 107-112, 1997.
[3] V. V. Abramov, B. S. Acharya, N. Akchurin, A. Ball, S. Banerjee, P. de Barbaro, et al., “Studies of the response of the prototype CMS Hadron Calorimeter, including magnetic field effects, to pion, electron, and muon beams,” Nucl. Instr. Meth. vol. A457, pp. 75-100, 2001.
[4] P. Cushman, A. Heering, and A. Ronzhin, “Studies of hybrid photomultiplier tubes in magnetic fields up to 5 Tesla,” Nucl. Instr. Meth. vol. A418, pp. 300-305, 1998.
[5] G. Anzivino, H. Arnaudon, P. Baillon, P. Benetti, L. Boskma, P. Burger, et al. “Review of the Hybrid photo diode tube (HPD) an advanced light detector for physics,” Nucl. Instr. Meth. vol. A 365, pp. 76-82, 1995.
[6] P. Cushman and R. Rusack, “A photomultiplier tube incorporating an avalanche photodiode,” Nucl. Instr. Meth. vol. A333, pp.381-390, 1993.
[7] A. Modinos, “Field, Thermionic and Secondary Electron Spectroscopy,” See p.20, p. 40 (Plenum, 1984)
[8] P. Benetti, C. Cattaneo, R. DeSalvo, V. Filippini, D. Grassi, M. Rossella, et al., “Speed properties of the hybrid photodiode tube,” Nucl. Instr. Meth. vo.l. A367, pp. 384-387, 1995.
[9] G. Lutz and A. S. Schwarz, “Silicon Devices for Charged-Particle Track and Vertex Detection,” Ann. Rev. Nucl. Part. Sci., vol. 45, pp. 295-335, 1995.
[10] E. H. Darlington, “Backscattering of 10-100 keV electrons from thick targets,” J. Phys. D 8, pp. 85-93, 1975.

[11] IMD Version 4.1.1, optical modeling package for multilayer structures by David L. Windt, http://cletus.phys.columbia.edu/windt/idl .

[12] P. Cushman, A. Heering, and A. Ronzhin, "Custom HPD readout for the CMS HCAL," Nucl. Instr. Meth. vol. A442, pp. 289-294, 2000.

[13] P. Cushman, A. Heering, and J. K. Nelson, "The effects of neutron irradiation on multi-pixel hybrid photodiode tubes," Nucl. Instr. Meth. vol. A411, pp. 304-312, 1998.